Applied Ocean Research 117 (2021) 102895

Contents lists available at ScienceDirect

Applied Ocean Research

journal homepage: www.elsevier.com/locate/apor

Empirical estimation of low-frequency nonlinear hydrodynamic loads on moored structures

Thomas Sauder *

SINTEF Ocean AS, P.O. Box 4762, Torgarden, Trondheim, 7465, Norway
Norwegian University of Science and Technology, Department of Marine Technology, Trondheim, 7491, Norway

ARTICLE INFO

Keywords:
Moored structures
Low-frequency motions
Model testing
Active positioning
Cross-bi-spectral analysis
Quadratic transfer function
Cyber–physical empirical method

ABSTRACT

Low-frequency (LF) motions of floating structures are commonly modeled as the response of an oscillator to a second-order wave excitation. We present here an empirical method that reliably estimates the oscillators parameters and quadratic transfer function (QTF) used in such models.

The method is based on an active stationkeeping system that enables to accurately control external boundary conditions applied on the floating structure in a wave basin. The resulting system can be successively tuned to different frequency ranges of interest. Then, by deconvolution and optimization, LF damping and added-mass loads, as well as a *response-independent* wave excitation load, can be evaluated. From the wave elevation, and estimated load time series, the difference-frequency QTF is finally estimated by a cross-bi-spectral analysis, including a new treatment of statistical noise.

The paper describes the proposed method in details, and illustrates it with the study of a ship-shaped floating unit in a sea-state of relevance for the fatigue design of mooring systems (steep waves, low return period).

1. Introduction

Large-volume moored structures have eigenfrequencies in the range 2–20 mHz, i.e.well below frequencies contained in the wave spectrum (50–200 mHz). They are usually associated with eigenmodes contained in the horizontal plane, i.e. combinations of surge, sway, and yaw. It is well-known that nonlinear terms in the wave-structure interaction problem yield wave loads at these low frequencies (Faltinsen, 1993, Chap. 5). For systems with little damping,[1] even if low-frequency wave loads are generally smaller in magnitude than wave-frequency loads, the resulting response of the floater can be significant near resonance. Quantifying low-frequency (LF) wave loads in severe sea-states (i.e. when the wave amplitude squared becomes comparatively large) is therefore a crucial step in the design of mooring systems, risers, power cables, and also for the heading stability of turret-moored structures. Common engineering practice is to approximate the hydrodynamic wave loading process on large-volume offshore structures as the sum of 1st and 2nd-order wave loads, in terms of the wave steepness, the 2nd-order component being expected to describe the LF excitation. The LF response, i.e. the displacement and heading, is then described as the response of a mechanical oscillator to this LF excitation. The mass term in this oscillator includes the structural mass and the asymptotic LF value of the added mass, and the stiffness corresponds to one of the positioning system. The LF damping results from viscous damping on the hull due to skin friction and flow separation, wave drift damping (more on this term later on), and damping induced by the riser system and positioning system. The contribution of each component to the total LF damping is very case dependent, and varies with the hull form, water depth, and sea-state, among others (Molin, 2002, Chapter 6). Our objective here is to model LF loads *on the floater only*, as an input to global analyses where subsea slender structures are modeled separately (Aksnes et al., 2015).

In the same way as linear wave loads are described by linear transfer functions, the 2nd order LF excitation on the floater is modeled by a difference-frequency Quadratic Transfer Functions (QTF) denoted $H^{(2)}$. It is a complex function linking the hydrodynamic load to a pair of incoming wave components with complex amplitude and frequency $(a_i, f_i)_{i=\{1,2\}}$ as follows. Assuming that $f_1 < f_2$, and defining the difference-frequency $\Delta f = f_2 - f_1$, the LF hydrodynamic load will occur at a frequency Δf, and its complex amplitude will be $2H^{(2)}(f_i, f_j)a_i a_j$. As a practical example, a difference-frequency QTF $H^{(2)} \equiv 1$ results,

* Correspondence to: SINTEF Ocean AS, P.O. Box 4762, Torgarden, Trondheim, 7465, Norway.
E-mail address: thomas.sauder@sintef.no.

[1] A notable example of such systems are a ship-shaped structures undergoing low-frequency surge motions in head seas, leading to insignificant wave radiation, and a damping ratio of a few percent.

https://doi.org/10.1016/j.apor.2021.102895
Received 27 May 2021; Received in revised form 3 August 2021; Accepted 21 September 2021
Available online 1 November 2021

in an irregular sea state, in a "load" equal to half of the amplitude square of the wave envelope: in other words, the 2nd order LF loading is in phase with the wave groups in this case. However, QTFs generally include an imaginary part (a phasing) which can be significant in shallow water, and exhibit amplitude variations over the bi-frequency (f_1, f_2) domain. This phasing with respect to the incoming wave is particularly important when it comes to capturing extreme loads in mooring lines, as these occur when large LF offsets (leading to a large "local" stiffness of the mooring system) are combined with large WF excitation.

1.1. Numerical and empirical QTF estimation methods

QTFs can be estimated numerically by 2nd order potential theory, where a perturbation method is applied, meaning that the wave steepness and motions are assumed to be asymptotically small. Examples of commercial programs currently implementing such methods are WAMIT, Hydrodstar, Wadam, AQWA and Orcawave. The computational burden associated with numerical estimations of *full* QTFs, i.e. over a wide range of the bi-frequency plane, used to be an issue. Various simplifying approximations were therefore developed, such as Newman or Pinkster approximations. See de Hauteclocque et al. (2012) and Engebretsen et al. (2020) for an overview and some important limitations of such approximations. With the computational power available nowadays, calculating full QTFs with the above-mentioned tools is now achievable in an engineering context, and such approximations become unnecessary. However, full QTFs obtained from potential theory do not always describe the hydrodynamic loading in a satisfactory way either. There are several reasons for this. (1) A significant contribution to the LF wave load is related to the wave-frequency (WF) relative wave elevation at the waterline (Pinkster, 1980, page 38). In many cases, the latter is affected by *viscous* drag loads, which are amplitude- and frequency-dependent. For example bilge keels increase the global WF heave or pitch damping on a ship by locally enforcing flow separation, and hereby influence the amplitude and phasing of her motions with respect to the incoming wave. LF wave loads are in turn affected as shown numerically in e.g. Engebretsen et al. (2020). They can therefore only be predicted correctly by potential theory if such amplitude- and frequency-dependent viscous effects are modeled correctly. (2) Wave–current interaction is not treated in a fully consistent way in 2nd order potential theory. The most prominent approximations are based on Aranha formula (1994) which corrects the LF load based on the wave frequency and relative LF velocity with respect to the current. Recently, another semi-empirical correction has been proposed by the EXWAVE project to account for wave–current interaction and sea-state dependency for semi-submersibles (Fonseca et al., 2017). It has also been applied, with promising results, to model wave-drift damping (Ommani et al., 2017). (3) The fundamental assumption of perturbation theory is that the 2nd-order (LF) motions are smaller in magnitude than the 1st-order (WF) motions. This assumption is violated for moored structures, as surge LF motions are typically an order of magnitude larger than WF motions. By Taylor expanding the LF wave excitation in the LF velocity and LF displacement, it appears that this violation results in a modification of the LF damping, stiffness and wave excitation (Molin, 2002, Chapter 6). A similar effect on the added mass is reported in Kinoshita et al. (2002) and Yoshida et al. (2005). While significant modifications of eigenfrequencies in harsh sea states have been reported for offshore structures, for example in Ommani et al. (2017), these are not fully understood and modeled yet. As of today, only the modification of LF damping is accounted for, through the so-called wave drift damping. (4) Finally, beyond-2nd order effects might lead to increased loads. Some of these effects can be categorized as "potential" effects, as they could in principle be modeled by a higher-order potential theory. An example is the additional load caused by a rapid change of geometry near the free surface, such as bow flares on ships. An other example is the couplings between yaw and other degrees of freedom, studied e.g. in Grue and Palm (1996). There are also known beyond-2nd order *viscous* effects, the most prominent example being obtained when integrating Morison-drag on columns up to the instantaneous free-surface. This results in 3rd-order loads in terms of wave amplitude (Faltinsen, 1993, p. 153).

In the harsh sea-states relevant for design, *empirical* estimation/correction of nonlinear wave loads is therefore necessary (Aksnes et al., 2015; Fonseca et al., 2017; Fonseca and Stansberg, 2017). Empirical methods consist in "observing" the response of the structure to a known incoming wave to infer the load it was subjected to. The state-of-the art approach for moored structures consists in model testing in hydrodynamic laboratories. In such a setting, the floater is kept in position by a horizontal mooring system connected to the basin sides. The stiffness of the mooring system in surge, sway and yaw is designed to be "soft", i.e. leading to natural periods well above the WF range, in order to minimize the effect on the WF motions of the floater. This system is then subjected to incoming waves representing a sea-state of interest, where the wave energy is usually concentrated around a peak period, and the resulting motions of the floater are recorded. From there, two types of methods are usually applied to estimate the LF wave loads. In the first case, the wave excitation loads are estimated from deconvolution of the motions by assuming a linear oscillator *with known parameters*. Then, from the load and the measured undisturbed input wave, QTFs are estimated using cross-bi-spectral analysis (see e.g. Pinkster (1979), Rugh (1981) and Stansberg (1997) for applications to marine hydrodynamics and Kim (2004) for a thorough literature study until 2004). The oscillator parameters are updated iteratively, until the reconstructed motions match with the measured ones. An alternative is to estimate the QTF and oscillator parameters by a least-square fitting of the response time series (Bunnik et al., 2006; Rogne et al., 2016). Such empirical methods are complementary to numerical methods, whose results might be confirmed (as it is generally the case in moderate sea-states), or corrected, as generally needed in harsher sea states, and/or in presence of current (Fonseca and Stansberg, 2017).

There are, however, also several limitations related to traditional empirical approaches, which are outlined in the following. (1) First of all, some systems such as FPSOs in head seas, have a small bandwidth, meaning that they respond mainly at their natural frequency. In that case, *proportional* variations of damping and excitation in the model result in very similar motion patterns. Such a "poor identifiability" property is often a challenge in numerical modeling, as one wishes to establish estimates of damping and excitation loads separately. (2) Then, once the soft mooring system is designed, the dynamical properties of the oscillator constituted by the floater in its mooring, including its eigenfrequencies, are fixed. If some of the LF load occurs at e.g. higher frequencies, the dynamical system might not respond significantly to it, filtering out relevant information about the loading. For this reason, the eigenfrequency of the soft mooring is often chosen to be the one of the *full-scale* system $f_{n,\text{field}}$. However, we will see in the following that this choice is not necessarily adequate. (3) Finally, soft mooring systems induce some (uncontrolled) damping due to drag loads on the portion of the lines in contact with water. This damping is usually small, but it can become significant when e.g. studying ships undergoing surge motions as the hull damping is small. This uncertainty reduces the accuracy of the deconvolution.

1.2. Main contributions, and structure of the paper

We present here a novel "cyber–physical" empirical method aimed at estimating LF hydrodynamic loads, and addressing the limitations listed above. A laboratory apparatus is presented in Section 2, that enables a precise control of external boundary conditions applied to the structure. Secondly, by exploiting this apparatus, we present, in Section 3, a method to estimate LF excitation forces, added-mass and damping forces *separately*, which is of importance for model calibration

purposes. The frequency range on which the LF excitation is estimated is also increased. And finally, in Section 4, we propose an improved way of establishing empirical QTFs from the estimate wave excitation time series. Here, domains of the bi-frequency plane where little information is available from the experiments are systematically identified and discarded. The presented method is illustrated with experiments involving a ship-shaped structure that had been studied thoroughly earlier (Fonseca and Stansberg, 2017).

2. Laboratory apparatus

The laboratory setup used in the present work consists in an active positioning system that applies a desired LF horizontal load $\tau_m \in \mathbb{R}^3$ (surge, sway, yaw) on the floating structure. The load τ_m can be chosen arbitrarily, but consists here of a restoring/damping load. It is calculated based on the *low-frequency* displacement/heading and velocities of the floater, estimated by an observer acting as real-time wave filter. The load τ_m is applied through a set of actuation lines with tensions $T = (T_1, \dots, T_n)$ where n is the number of actuators. See Fig. 1 for a setup with $n = 6$ actuators. The block diagram in Fig. 2 shows the control architecture of the setup presented here. The setup has been briefly presented earlier in Sauder and Tahchiev (2020).

Before describing in details this setup, we would like to pinpoint that using an active positioning system to estimate LF wave loads is not a new idea. It was actually suggested more than 40 years ago (Pinkster, 1980, page 111), and some more details about the practical implementation were given in Pinkster and Huijsmans (1992). The objective at that time was to *totally restrain* LF motions, while ensuring free WF motions. The applied forces when doing so would be measured, and be the exact opposite of the sought LF loads. Restraining LF motions was performed by a feed-forward controller using instantaneous relative wave elevation measurements at several places around the ship to estimate LF forces. The feed-forward controller was completed by a feedback controller. As they still were spurious residual LF motions present, these were transformed into loads using *assumed* added mass and damping coefficients, and subtracted from the estimated LF loads. Note that this setup, by construction, could not provide information about LF added-mass and damping loads themselves. Not much details were given regarding the performance of the setup, and it is unclear whether this setup has been used later on. To the author's knowledge, no other similar setups has been developed by others.

We will in the following, detail the different components of the setup as presented in Fig. 2, starting from the physical model.

The physical model used in the present study is the Floating Production, Storage and Offloading unit (FPSO) already studied in details in Fonseca and Stansberg (2017) and other publications by the same authors. The FPSO model was manufactured at a scale of $\lambda = 1/70$, and ballasted to its fully loaded condition. Main particulars and key parameters of the FPSO are provided in Table 1. The full scale water depth was 210 m, i.e. 3 m at model scale. The model was installed in the Ocean Basin at SINTEF Ocean, and subjected to waves. The instrumentation of the model consisted of (1) an optical motion tracking system with sampling frequency of 100 Hz, and (2) line tension measurements for all lines connected to the model, visible on Fig. 1, with sampling frequency of 200 Hz, and low-pass filtering at 20 Hz.

2.1. Estimation of LF position and velocity

The measurements coming from the optical motions tracking contain both the LF component and the wave frequency-range component of the motions. To obtain real-time estimates of the LF position/heading and velocity in real-time, we use a model-based wave-filtering technique widely used in dynamic positioning (DP) systems.

The conventions and notations for coordinate systems described in Fossen (2011) are adopted here (see also Fig. 1). Assuming that there is a clearly separated frequency content for WF and LF motions, let

Table 1
FPSO main particulars (scale 1/70), mass and stability properties.

Parameter	Unit	Model scale	Full scale
Length over all	[m]	3.663	256.4
Length betw. perpendiculars	[m]	3.486	244.0
Beam	[m]	0.686	48.0
Draught	[m]	0.380	26.6
Displacement	[kg], [t]	507.3	178 365
Vertical CoG above baseline	[m]	0.269	18.83
Longitudinal CoG fwd of AP	[m]	1.711	119.8
Transverse metacentric height	[m]	0.0322	2.254
Radius of gyration in roll	[m]	0.223	15.61
Radius of gyration in pitch	[m]	0.768	53.76
Natural period — heave	[s]	1.4	11.5
Natural period — roll	[s]	2.7	22.7
Natural period — pitch	[s]	1.2	9.6

$\eta = [N, E, \psi]$ be the LF-component of the position/attitude vector of the body in the inertial frame of reference, equipped with a North-East-Down coordinate system. Let $\nu = [u, v, r]$ be the LF-component of the body linear/angular velocity, expressed in a body-fixed frame of reference (surge, sway, yaw). Let $R(\psi)$ be the rotation matrix converting body-fixed vector coordinates into coordinates expressed in the inertial frame of reference. The motions of the floater in its mooring can be approximated by the following set of equations:

$$\eta = R(\psi)\nu \tag{1}$$

$$M\dot{\nu} + C(\nu)\nu + D\nu = \tau_m(\eta) + \tau_w(t) \tag{2}$$

In this equation, the mass term $M \in \mathbb{R}^{3\times3}$ consists of the sum of the mass and LF-asymptotic value of the added mass, estimated e.g. from potential flow theory. The linearized damping matrix $D \in \mathbb{R}^{3\times3}$ can be obtained from free decay tests, as presented in Sauder and Tahchiev (2020). The Coriolis-centripetal term $C(\nu)\nu$ can be neglected here since LF velocities are small. τ_m is the force applied by the active positioning system and $\tau_w(t)$ is the LF wave excitation force.

Online wave filtering (estimation of η), and estimation of ν, are performed with the nonlinear passive observer (Fossen and Strand, 1999) described in the following. Denoting $\eta_w \in \mathbb{R}^3$ the WF component of the position/heading, y the measurement of $\eta+\eta_w$, and $\hat{y}$ its estimated counterpart, the estimation error (also known as the *innovation*) is defined as $\tilde{y} = y - \hat{y}$. The following equations describe the WF motion estimator:

$$\hat{y} = \hat{\eta} + C_w\hat{\xi} \tag{3}$$

$$\dot{\hat{\xi}} = A_w\hat{\xi} + K_1\tilde{y} \tag{4}$$

where $\xi \in \mathbb{R}^6$ is the state vector of a 3-degrees of freedom linear oscillator, such that $C_w\xi$ models the WF response. The matrices $A_w \in \mathbb{R}^{6\times6}$ $C_w \in \mathbb{R}^{3\times6}$ and $K_1 \in \mathbb{R}^{6\times3}$ are selected based on the floater's resonance frequencies, damping ratios, and sea-state peak period (see Fossen, 2011, Chapter 11 for details), which, in a laboratory setting, are well defined. Estimates of the LF position, heading and velocity are given by

$$\dot{\hat{\eta}} = R\hat{\nu} + K_2\tilde{y} \tag{5}$$

$$M\dot{\hat{\nu}} = -D\hat{\nu} + R^\top\hat{b} + \tau_m + R^\top K_4\tilde{y} \tag{6}$$

$$\dot{\hat{b}} = -T_b^{-1}\hat{b} + K_3\tilde{y} \tag{7}$$

where (5) and (6) copy the kinematic and dynamic equations of motions given in (1) and (2), respectively, and where (7) the estimates slowly-varying biases, including LF wave loads. $T_b \in \mathbb{R}^{3\times3}$ is a diagonal matrix of positive time constants, that will low-pass filter the bias variations. All gains matrices $K_{\{2,3,4\}}$ have a diagonal structure, and are selected to satisfy passivity constraints, and hence ensure convergence of the estimation error to zero. The interested reader is referred to Fossen (2011, Chapter 11) for more details. Delays introduced in the control loop by calculation time, data processing and transport time,

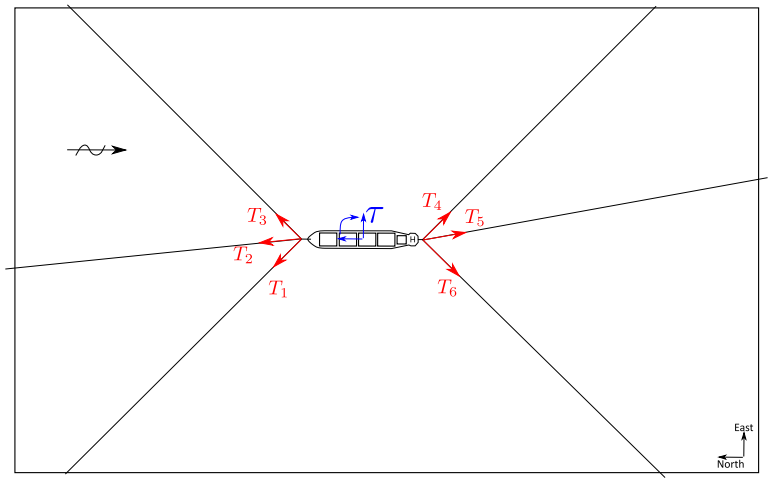

Fig. 1. Active positioning system — Setup in the Ocean Basin, including the earth-fixed North-East-Down coordinate system, the forces applied by the positioning system (in red) and resulting load vector τ (in blue) expressed in the body-fixed coordinate system. Notations are consistent with those presented in Fossen (2011).

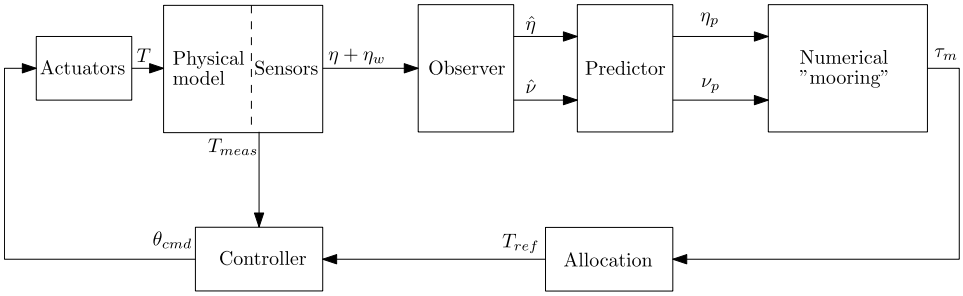

Fig. 2. Active positioning system — Block diagram. See main text for notations.

are estimated offline using cross-correlation, and the observed values $\hat{\eta}$ and $\hat{\nu}$ are predicted using polynomial forward prediction (Vilsen et al., 2017). Predicted values η_p and ν_p (20 ms ahead) are then used as estimates of η and ν in the following.

2.2. Applying restoring and damping loads

The load vector applied by the active positioning system on the floater consists in a linear anisotropic restoring and damping load, formulated as:

$$\tau_m = -R(\psi)^\top R(\alpha_m)\left[D_m R(\alpha_m)^\top R(\psi)\nu + K_m R(\alpha_m)^\top(\eta - \eta_{\text{ref}})\right] \tag{8}$$

where α_m defines a main axis direction with respect to North, and $K_m = \text{diag}(k_i, k_t, k_{\text{rot}})$ and $D_m = \text{diag}(d_i, d_t, d_{\text{rot}})$ contain the inline, transverse, and rotational stiffness and damping terms, respectively. The equilibrium point is defined by $\eta_{\text{ref}} = (N_0, E_0, \psi_0)^\top$.

Then, given desired a load vector τ_m, the allocation block in Fig. 2 computes the tension that should be exerted by each cable on the ship. Let $T_0 \in \mathbb{R}^6$ be a tuple containing a pretension for each of the six lines depicted in Fig. 1, in our case 15 N. Let $\Delta T \in \mathbb{R}^6$ be the additional tension allocated on each line in order to achieve the correct load vector. We denote $A_c(\eta)$ the configuration matrix, which depends on the actuators position, body position, and position of the attachment point of the lines on the body (Vilsen et al., 2017). Given T_0, we obtain ΔT from the Moore–Penrose pseudo-inverse of A_c, which leads to a minimum deviation $|\Delta T|^2$ to the pretension:

$$\Delta T = A_c^\dagger(\tau - A_c T_0) \tag{9}$$

For some configurations, for example when large heading are investigated with the setup presented in Fig. 1, it is beneficial to adapt the pretension T_0 to avoid that lines go slack. This is done automatically by the following adaption law:

$$\dot{T}_0(t) = K_{T_0}\int_0^t \left(\frac{\max_{i=\{1,2,\dots,6\}}\left(T_0(t') + \Delta T_i(t')\right) + \min_{i=\{1,2,\dots,6\}}\left(T_0(t') + \Delta T_i(t')\right)}{2} - T_{0,target}\right) dt' \tag{10}$$

which moves the envelope of the tensions away from the extreme tension values. The gain K_{T_0} is used to tune the speed of the adaptation.

The desired line tensions are applied on the structure by using a set of six custom-made actuators designed at SINTEF Ocean. They consist in off-the-shelf rotary brushless servomotors, connected, with some compliance, to the drum around which the lines are twined. The compliance is obtained by using a clock spring with known stiffness. A tension controller, represented in Fig. 2 defines the desired shaft angle θ_{cmd} of the servomotor. The control objective for the tension controller is twofolds: (CO1) Track of the commanded LF tensions originating from the allocation module, and (CO2) reject WF disturbances, meaning that the line tensions should not be influenced by FPSO motions at WF. To achieve this objective, the controller consists of three terms: (T1) a feed-forward term that converts change in desired LF tensions to changes in the shaft angle, which contributes to (CO1). (T2) The second term in the controller maps the rotations of the drum to the angle of the shaft hereby avoiding any spurious force as requested by (CO2). The third term (T3) of the controller is a feedback term that aims at canceling remaining errors. More details regarding the mechanical design of the actuators and their controller are given in Ueland et al. (2021). With the present setup, the typical accuracy of the force tracking was on the order of 0.1 N.

2.3. Conclusion

It has been shown earlier that the presented active positioning system is able to replicate tests obtained with a passive soft mooring system (Sauder and Tahchiev, 2020). The complete validation study described in this reference (and not repeated here), included static excursion tests, decay tests, and tests in irregular waves.

To summarize, the setup presented here enables to conveniently apply a freely-chosen linear restoring and damping load based on LF motions only. As opposed to traditional soft mooring systems, the external load is perfectly deterministic as the tension in the lines are feedback controlled at the attachment points on the model. The presented setup also enables automatic heading changes and decay tests by simply adjusting η_{ref}. The anisotropic characteristic of the stiffness and damping enables to study or mitigate the effect of couplings, by associating a comparatively larger damping level to LF yaw motions for example.

3. Estimation of LF hydrodynamic loads

In this section, we show how the laboratory setup presented in Section 2 enables to efficiently estimate the LF added mass and damping coefficients, and LF wave excitation loads over a wide range of frequencies. Without loss of generality, we assume now that the motions of the system are decoupled, and that the LF motions can be described by the following scalar linear equation, where the quantities to be estimated are in red:

$$(m+a)\ddot{\eta}(t) + d_h\dot{\eta}(t) = \tau_w(t) + \tau_m(\eta,\dot{\eta}) \tag{11}$$

Let $\tau_m(\eta,\dot{\eta}) = -d_m\dot{\eta} - k_m\eta$, be the (known) load applied by the apparatus described in Section 2, (11) becomes:

$$(m+a)\ddot{\eta}(t) + (d_h+d_m)\dot{\eta}(t) + k_m\eta(t) = \tau_w(t) \tag{12}$$

The parameters in blue can be freely adjusted, and quantities in black can be measured or derived in a post-processing phase. Assume now that we perform a set of N_{tests} tests using the same incoming wave, but where parameters in τ_m are varied,. We obtain the following set of equations: $\forall i \in \{1,\dots,N_{\text{tests}}\}$,

$$m\ddot{\eta}^{(i)}(t) + d_m^{(i)}\dot{\eta}^{(i)}(t) + k_m^{(i)}\eta^{(i)}(t) = \tau_{\text{tot}}^{(i)} \tag{13}$$

$$\text{where } \tau_{\text{tot}}^{(i)} = \tau_w(t) - a\ddot{\eta}^{(i)}(t) - d_h\dot{\eta}^{(i)}(t) \tag{14}$$

This equation now represents an oscillator with *known* parameters, excited by a force $\tau_{\text{tot}}^{(i)}$ that can accurately be determined by deconvolution (more details will be given in 3.2 about this). Now, according to the postulated model (2), the wave excitation $\tau_w(t)$ should not vary much from test to test, while part of the loading, namely the added mass $-a\ddot{\eta}(t)$ and damping loads $-d_h\dot{\eta}(t)$ are response-dependent, and will vary with varying d_m and k_m. Hence, the LF added mass and damping can be estimated by solving the following minimization problem:

$$(\bar{a},\bar{d}_h) = \arg\min_{a,d_h} \int_0^T \text{Var}_{i=\{1,\dots,N_{\text{tests}}\}}[\tau_{\text{tot}}^{(i)} + a\ddot{\eta}^{(i)}(t) + d_h\dot{\eta}^{(i)}(t)]dt \tag{15}$$

where $\text{Var}_{\{\dots\}}$ denotes the variance over the set of tests and T the test duration. Once the optimal parameters $\bar{a}$ and $\bar{d}_h$ are found, they can be used to determine the excitation force as

$$\tau_w(t) = \text{E}_{i=\{1,\dots,N_{\text{tests}}\}}[\tau_{\text{tot}}^{(i)} + \bar{a}\ddot{\eta}^{(i)}(t) + \bar{d}_h\dot{\eta}^{(i)}(t)] \tag{16}$$

where $\text{E}_{\{\dots\}}$ denotes the average over the set of tests. The *variance* of the same quantity provides an indication about how well the model structure (11) suits the problem at hand.[2] In the following, we will first illustrate this approach with an example before providing more insight about the selection of the $k_m^{(i)}$ and $d_m^{(i)}$ parameters, and test duration.

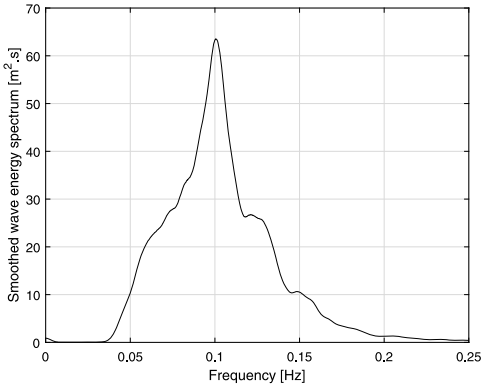

Fig. 3. Wave spectrum.

3.1. Example

We consider the FPSO described in Section 2 in head seas. The significant wave height is $H_s = 7.3$ m, and the peak period $T_p = 10.0$ s. The wave energy spectrum (JONSWAP) is presented in Fig. 3. Such a sea-state is typically of importance when estimating fatigue damage on mooring lines, as it is energetic and occurs with a relatively high frequency in the Norwegian Sea. Furthermore, it is interesting for the purpose of the present research, as (1) it is rather steep, with $2\pi H_s/(gT_p^2) \simeq 0.05$, meaning that weakly nonlinear effects such as 2nd-order wave loads should be significant, and (2) because T_p is in the vicinity of the heave and pitch natural periods (see Table 1), where the surge component of the difference-frequency QTF is usually large and/or exhibits large variations. On the other hand, the sea-state is not extreme, in the sense that green-water or bow-flare slamming do not occur much during the tests (confirmed by video footage during the present study). This means that 2nd-order potential theory also provides adequate estimates of the LF wave loads for this sea-state (Fonseca and Stansberg, 2017), which adds a useful reference to benchmark the present empirical estimation method.

Five tests ($N_{\text{tests}} = 5$) were performed, with a full-scale duration $T = 14223$ s each. The values of $k_m^{(i)}$ and $d_m^{(i)}$ used in each test are reported in Table 2. In tests 1–3 the damping d_m increased, while the stiffness remained close to its nominal value $k_m = 268$ kN/m. In tests 4 and 5 the stiffness k_m varied, while keeping the damping close to its nominal value $d_m = 315$ kN/(m/s). The resulting motions of the floater for the five cases are plotted in black in Fig. 10. It is clear that the frequency content and amplitude of the motion varies significantly from test to test.

Applying the method described above, the resolution of (15) results in identified parameters $\bar{a} = 12.29$ t, i.e. a LF added-mass in surge of about 7% of the structural mass, and a linearized LF damping of $\bar{d}_h = 302$ kN/(m/s), which corresponds to a damping ratio of 2% for the full-scale asset. These results are in good agreement with results established independently by Fonseca and Stansberg (2017). The value of the cost function in (15) is presented in Fig. 4. The estimated excitation force time series τ_w(t), estimated from (16), is also represented in Fig. 4. It can be seen that the standard deviation of the estimated τ_w across the tests is very small, which validates the model structure

[2] One reason for which the model structure (11) might not be valid has been discussed in Section 1.1, and is related to the fact that τ_w might be affected by the non-infinitesimal character of the LF response. So, while achieving a perfectly consistent wave loading across all cases (i.e. a zero variance) should not be expected in general, a sufficiently small variance supports the validity of the assumed structure of Eq. (11).

Table 2
Parameters $k_m^{(i)}$ and $d_m^{(i)}$ used in each test, and corresponding natural frequency f_n and damping ratio ζ. The listed eigenfrequencies f_n correspond to periods $1/f_n$ equal to 162 s, 240 s and 96 s, respectively..

i	$k_m^{(i)}$ kN/m	$d_m^{(i)}$ kN/(m/s)	f_n mHz	ζ %
1	268	315	6.16	2.3
2	267	924	6.16	6.7
3	267	2231	6.16	16.2
4	122	311	4.17	3.3
5	763	324	10.41	1.4

(11). The frequency content of the estimated force is not significant for frequencies larger than 12 mHz (i.e. periods less than 83 s).

3.2. Deconvolution, and choice of $k_m^{(i)}$ and $d_m^{(i)}$

Estimating τ_{tot} in (13) from the measured motions and known parameters k_m and d_m consists in performing a linear deconvolution. In the frequency domain, it simply means that the Fourier coefficients of τ_{tot} are obtained by dividing the Fourier coefficients of η by the complex transfer function

$$H(f|k_m, f_n, \zeta) = \frac{1}{k_m} \cdot \frac{1}{1 - \left(\frac{f}{f_n}\right)^2 + 2i\zeta\frac{f}{f_n}} \tag{17}$$

where $2\pi f_n = \sqrt{k_m/m}$ and $\zeta = d_m/\sqrt{2k_m m}$. We will refer to the amplitude of this transfer function, as the *sensitivity* σ of the setup. Fig. 5 presents σ for each of the five tests conditions in Table 2.

The following important considerations about the choice of $k_m^{(i)}$ and $d_m^{(i)}$ can be made. First of all, the setup should have a low sensitivity in the WF range, or near natural frequencies of the floater in the WF range (typically modes involving heave, roll, and pitch). An important reason for this, discussed in the introduction, is that LF loads depend on WF motions, which should be left undisturbed. This criterion is also related to the fact that one wishes to clearly separate by filtering the LF motions from the WF motions in post-processing. In the present setup (head seas), one wishes σ to be negligible beyond 87 mHz, which is the heave eigenfrequency.

Then, σ should be high enough so that the response, i.e. the displacement amplitude, is greater than position/heading measurements uncertainty at frequencies of interest (here 0–12 mHz). This requirement can be quantified as follows. Let $(\delta\tau)_{\min}$ be the order of magnitude of the force that one wishes to measure at full scale, and $(\delta\eta)_{\min}$ the order of magnitude of the measurement error at model scale, then[3]

$$\sigma \geq \sigma_{\min} :\simeq \frac{(\delta\eta)_{\min}}{(\delta\tau)_{\min}\lambda^3} \tag{18}$$

In the present example, setting $(\delta\tau)_{\min} = 100$ kN and $(\delta\tau)_{\min} = 5$ mm (i.e. requesting that a load of 100 kN at full-scale triggers a displacement at least of 5 mm at model scale) leads to a minimum acceptable sensitivity of $\sigma_{\min} = 17$ mm/N, which is greyed on in Fig. 5. One clearly sees that relying on one single oscillator (among those considered here) only will not lead to a sufficient sensitivity throughout the full frequency range of interest (0–12 mHz), while the combination of cases studied here covers this range.

On the other hand, it is not necessarily favorable to *maximize* the sensitivity by excessively reducing d_m and hence ζ. Indeed, in case there is some uncertainty on the natural frequency f_n (due to measurement inaccuracies on the mass or moments of inertia for example), performing a deconvolution with a very little damped oscillator might lead to significant errors in the estimated loading near f_n. This error can be quantified by looking at

$$\frac{\tau_{\text{est.}}}{\tau_{\text{true}}} = \frac{H(f|k_m, f_n, \zeta)}{H(f|k_m, (1+\varepsilon)f_n, \zeta)} \tag{19}$$

illustrated in Fig. 6. This plots shows, for the three eigenfrequencies in Table 2, and four representative damping ratios, the estimated amplitude and phase error on the estimated force caused by a $\varepsilon = 2\%$ error on the assumed f_n. Note first that an error in the assumed f_n causes a constant error of about 2ε on the whole frequency range beyond f_n. Furthermore, the error in the estimated force amplitude and phase is maximal around f_n, and can be significant for systems with small d_m. This indicates that f_n should, in principle, not be chosen too close to the natural frequency of the floater *in its mooring in the field* $f_{\text{n,field}}$, as it is precisely around this frequency that the excitation forces should be estimated accurately.

As a final remark, when studying systems with much hydrodynamic damping d_h, which is typically the case for semi-submersibles, the resulting load $\tau_w(t)$ might be dominated by damping loads $-d_h\dot{\eta}$, leading to small motions. The present setup enables to compensate for this by selecting *negative* d_m values which is not feasible using a traditional passive soft mooring setup.

3.3. A note on test duration, and conclusion

The frequency resolution $(\Delta f)_{\min}$ of the motion and load spectra is directly related to the test duration T by $(\Delta f)_{\min} = 1/T$, which is equal to 0.07 mHz in the present example. In other words, the frequency range of interest for nonlinear LF wave loads, here 12 mHz wide, is described by 170 points. It is important to be aware of this when smoothing power spectra such as the one presented in Fig. 4.

Defining the minimum test duration based on the problem at hand can hence be done based on two criteria. (1) there should be enough points in the "very low"-frequency range up the natural frequency of the full-scale system $f_{\text{n,field}}$, i.e. $f_n T > A_1$, where A_1 is large, typically of the order of 100. (2) the LF load spectrum should be resolved correctly in the vicinity of $f_{\text{n,field}}$. This constraint relates to the damping ratio of the full-scale system ζ_{field}, and hence its quality factor/bandwidth: $2\zeta_{\text{field}} f_{\text{n,field}} T > A_2$, where A_2 is of the order of 10–100. The value of $T = 14423$ s used in the present study leads to an acceptable frequency resolution for the system at hand.

To conclude, we have in this section shown how the apparatus presented in Section 2 enables an independent estimation of the LF added mass, damping, and excitation load τ_w. The estimated hydrodynamic loads are valid across several tests where the LF motions vary significantly, which shows the validity of the linear model structure in (11) for the case at hand. We also provided guidelines for the choice of $k_m^{(i)}$ and $d_m^{(i)}$ to be applied in the tests, depending on the full-scale natural periods of the system of interest, the expected level of hydrodynamic damping, and the LF frequency range of interest.

4. Estimation of difference-frequency QTFs

In the previous section, a LF wave excitation load *time-series* $\tau_w(t)$ for $t \in [0, T]$ was estimated. The objective is now to extract an empirical QTF $H^{(2)} : \mathbb{R}^2 \to \mathbb{C}$, that could relate the undisturbed wave time series $x(t)$ to $\tau_w(t)$ for other realizations of similar sea states.

4.1. Cross-bi-spectral analysis

Let $X(f)$ denote by the double-sided Fourier transform of $x(t)$. We have $x(t) = \int_{-\infty}^{\infty} X(f) e^{i2\pi f t} df$ We assume that $X(f)$ is a complex Gaussian (i.e. circularly distributed) random variable with zero mean, and that the components of $X(f)$ at any two frequencies spaced by more than $1/T$ are statistically independent (Bendat and Piersol, 2010, eq (11.114)). We define the power spectrum as $S_{xx}(f) = \frac{1}{T}\langle X^*(f)X(f)\rangle = \frac{1}{T}\langle |X(f)|^2\rangle$ where the brackets denote the mathematical expectation.

[3] Density ratios are neglected, and we remind that $\lambda < 1$.

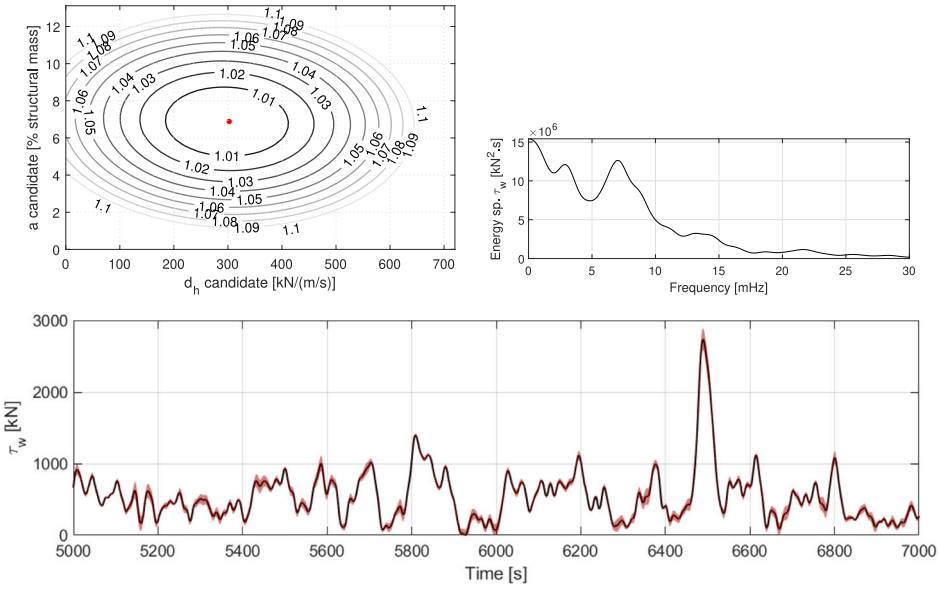

Fig. 4. Top left: cost function in (15) (normalized by minimizer value), and minimizer $(\bar{a}, \bar{d}_h)$ represented in red. Bottom: LF force estimated from (16) ± one standard deviation of the estimated τ_w across the tests. Top right: power spectrum of τ_w.

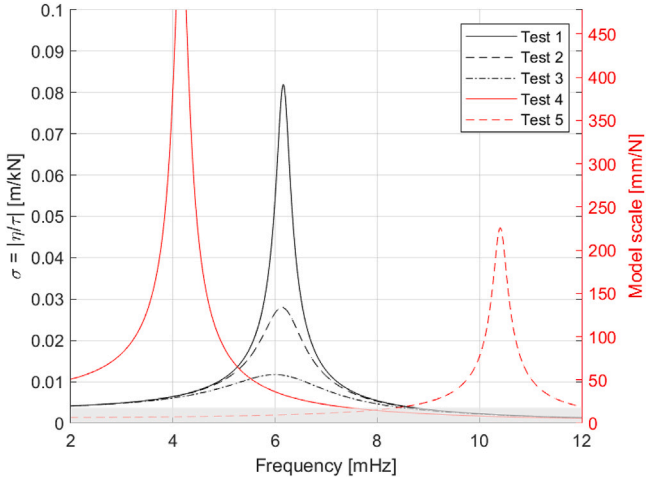

Fig. 5. Sensitivity of the system as defined in (17) for the mooring stiffness and damping parameters in Table 2.

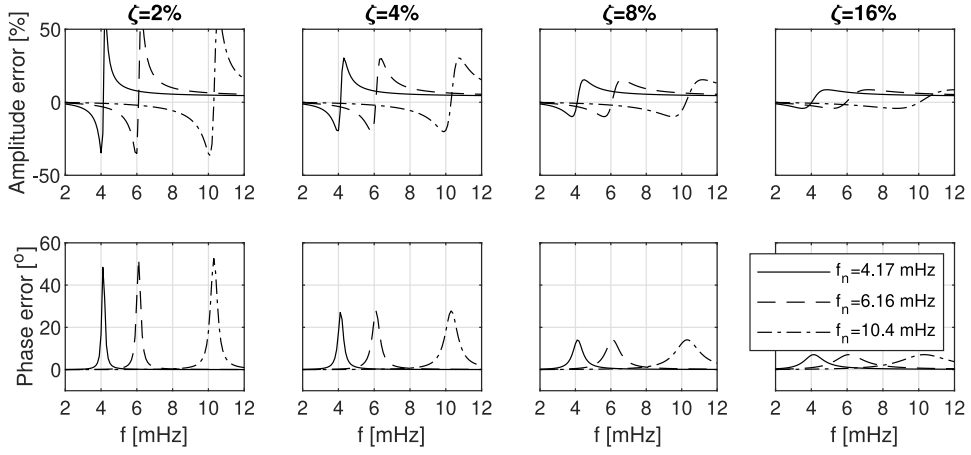

Fig. 6. Consequence of a 2% error on the assumed natural frequency in the deconvolution. Amplitude (top) and phase (bottom) of the error shown for systems with various eigenfrequencies (3 curves) and damping ratios (4 columns).

In this section, we will denote the force $y(t)$, instead of τ_w, as it is the typical notation used for *outputs* in signal processing. The definitions of important terms used in the following are given in Table 3. This table also draws a parallel between concepts used in linear signal analysis with which most readers are familiar with, and second-order signal analysis. Note that the notations used herein are consistent with Volterra series expansions (e.g. use of the four quadrants of the bi-frequency plane to describe the quadratic loads), that differ slightly from other conventions, where y is computed by a double sum over positive frequencies only. We define the mean frequency $f_0 = (f_1 + f_2)/2$ and the difference frequency $\Delta f = f_2 - f_1$. Note that the variable change $(f_0, \Delta_f) \leftrightarrow (f_1, f_2)$ has a Jacobian determinant of 1, meaning that integration over the bi-frequency domain of functions of (f_1, f_2) or $(f_0, \Delta f)$ are equivalent.

The empirical QTF $H^{(2)}$ is estimated by using Eq. (28) in Table 3. The power spectrum of the output (LF wave loading) S_{yy} can be found from (30). To illustrate the mechanisms at play in these equations, proofs are provided in Appendices B and C, respectively. Noteworthy, two assumptions are crucial to obtain these results: that the relationship between x and y should purely second-order, and the components of $X(f)$ at any two frequencies spaced by more than $1/T$ should be uncorrelated.

Deriving $H^{(2)}$ from (28) also requires an estimate of the cross-bi-spectrum S_{xxy}, defined in (26) as a mathematical expectation. Due to the stochastic nature of the wave process, a number of realizations of $x(t)$ and $y(t)$ tending to infinity[4] would be needed to converge towards S_{xxy}. In practice, only one or a few time series are available, defined on a finite window $t \in [0, T]$. It has however been shown that averaging over n_d adjacent frequency components from a single record of total length $T = n_d T_r$ is equivalent (in terms of random error in the estimate) to averaging over n_d different records, each of reduced length T_r (Bendat and Piersol, 2010, section 11.5). In other words, the estimation of mathematical expectation of S_{xxy}, and hence $H^{(2)}$, by smoothing sets a stringent requirement on a sufficiently large test duration T. This requirement comes in addition to those discussed in Section 3.3, related to the wave load estimation. In the present work, the smoothing was performed by convolution with a Gaussian envelope, as previously described in Stansberg (1997).

4.2. Denoising of the QTF

Several authors have noted that, when $x(t)$ has a relatively narrow-banded spectrum, then $H^{(2)}$ is estimated accurately only for mean frequencies f_0 near the peak of spectrum (Pinkster and Huijsmans, 1992; Stansberg, 1997). This is due to the fact that the variance of the raw cross-bi-spectrum χ increases fast, in comparison with $\langle \chi \rangle$ when S_{xx} decreases (Stansberg, 1997, page 9). We propose to deal with this issue as follows. Based on Eqs. (19) and (22) in Stansberg (1997), we define the estimated signal-to-noise ratio of the cross-bi-spectrum as

$$\xi(f_1, f_2) = |H^{(2)}(f_1, f_2)| \sqrt{\frac{S_{xx}(f_1) S_{xx}(f_2)}{T \cdot S_{yy}(\Delta f)}} \tag{32}$$

We then cancel (set to zero) all components of $H^{(2)}$ for which $\xi < \xi_{\min}$, where $\xi_{\min}$ is a minimum signal-to-noise ratio defined by the analyst. In other words, we enforce no contribution from the QTF to the output (wave loads) from areas in the bi-frequency plane where we lack information to estimate the QTF properly. In reality, there might be some contribution elsewhere in the bi-frequency plane, so, by "pruning" the QTF, we generally remove energy from the reconstructed output signal. A heuristic way of alleviating this is therefore to re-scale $H^{(2)}$, so as to match exactly the energy content of the output for each difference-frequency, which can formally be written as:

$$\forall \Delta f > 0, H^{(2)}(f_0, \Delta f) \leftarrow H^{(2)}(f_0, \Delta f) \sqrt{\frac{S_{yy,\text{measured}}(\Delta f)}{S_{yy,\text{estimated}}(\Delta f)}} \tag{33}$$

It should be noted that several authors suggest to assess and possibly alleviate the effect of statistical noise on $H^{(2)}$ estimates, by using the Hilbert transform $x_H(t)$, and more particularly the complex analytic signal $x_A(t) = x(t) + i x_H(t)$, whose module is the wave envelope (Pinkster and Huijsmans, 1992; Stansberg, 1997). Indeed, applying a unit difference-frequency QTF $H_u(f_1, f_2)$ to the input wave signal $x(t)$, yields an output equal to $|x_A(t)|^2/2$ (proof given in Appendix D). So comparing H_u, estimated from the pair $(x(t), |x_A(t)|^2/2)$, with the unit difference-frequency QTF, can provide some information about the quality of the estimate of $H^{(2)}$ obtained from the pair $(x(t), y(t))$. This assessment is useful to detect where assumptions discussed in Section 4.1 might be violated. A possibility is then to re-normalize the $H^{(2)}$ by H_u, which was not found necessary here.

4.3. Benchmark of the procedure against a known QTF

In order to verify the procedure above on a purely 2nd-order process, we define the following QTF, with bell-shaped amplitude, and a phase linearly varying with difference-frequency: $\mathcal{H}^{(2)}(f_1, f_2) = \mathcal{A}(f_1, f_2) e^{i\mathcal{P}(f_1, f_2)}$ where

$$\mathcal{A}(f_1, f_2) = \mathcal{A}_0 \exp\left(-\frac{(f_1 - f_b)^2}{2\sigma_b^2} - \frac{(f_2 - f_b)^2}{2\sigma_b^2} \right) \tag{34}$$

and $\mathcal{A}_0 = 100$ kN/m^2, $f_b = 0.1$ Hz, $\sigma_b = 7.96$ mHz, and $\mathcal{P}(f_1, f_2) = (f_1 - f_2) \times 67.8 \times 10^{-3}$[°/Hz]. The same wave time series $x(t)$ as used in Section 3, is used, with $T_p = 1/f_b$. The QTF estimation procedure including reconstruction of the time series takes one second on a common laptop.

The estimated QTF is compared, in Fig. 7, to $\mathcal{H}^{(2)}$ for three values of the difference frequency. Two correspond to lower and upper periods "bounds" of 100 s and 250 s that are relevant for typical offshore systems. The third one, corresponds to 169 s, which is the natural period in surge of the actual asset described in Section 2. According to the proposed method, the QTF estimate is made only for bi-frequencies at which $\xi(f_1, f_2)$ was larger than the upper 10th percentile of ξ. This results in a rather narrow band of 0.02 Hz, centered on $1/T_p = 0.1$ Hz. The match in the amplitude is acceptable, with an error on the order of 10%. The error on the phase is of the order of 15° .

It can be noticed that the relative error in amplitude and phase increases with increasing Δf, which can be explained by the fact that for a "peaky" spectrum such as the one used here (see Fig. 3), $S_{xx}(1/T_p) S_{xx}(1/T_p + \Delta f/2)$, and thus ξ, decrease fast with Δf. Note also that the amplitude $\mathcal{A}(f_1, f_2)$ of our benchmark QTF also decreases in module with Δf. The original and reconstructed output are compared in Fig. 8. As (33) has been applied, their spectra agree well by construction. Differences between the reconstructed output time series can be noticed, originating from the truncation of the QTF and the estimation errors described above, but the main features of the time series are well captured. The L^2 error between the time series is of 5.1%, and the amplitude of the maxima are reasonably well captured. The estimation would be acceptable in an engineering context.

4.4. Application to the FPSO

The same procedure is applied to $y(t) = \tau_w(t)$, the surge force on the FPSO estimated in Section 3, based on the same wave input $x(t)$. The estimated empirical QTF is compared to results obtained with 2nd order potential theory by the EXWAVE project (Fonseca and Stansberg, 2017). Results are shown in Fig. 9. Compared to the analytical case in the previous section, the support of $H^{(2)}$ is about twice wider, and it results on a wider range of ξ values, even if S_{xx} is the same as in

[4] Or an infinitely long testing period if one assumes ergodicity.

Table 3
Definitions of terms, and parallels between concepts used in first- and second-order process analysis.

Linear analysis		Quadratic analysis	
Linear Transfer Function (LTF)		Quadratic Transfer Function (QTF)	
$y^{(1)}(t) = \int_{-\infty}^{\infty} H^{(1)}(f)X(f)e^{i2\pi ft}df$	(20)	$y^{(2)}(t) = \iint_{-\infty}^{\infty} H^{(2)}(f_1,f_2)X^*(f_1)X(f_2)e^{i2\pi(f_2-f_1)t}df_1df_2$	(21)
		$y^{(2)}(t) = \int_{-\infty}^{\infty}\left(\int_{-\infty}^{\infty} H^{(2)}(f_0,\Delta f)X^*(f_0-\frac{\Delta f}{2})X(f_0+\frac{\Delta f}{2})df_0\right)e^{i2\pi\Delta ft}d\Delta f$	(22)
Fourier coefficient output		Fourier coefficient output	
$Y^{(1)}(f) = H^{(1)}(f)X(f)$	(23)	$Y^{(2)}(\Delta f) = \int_{-\infty}^{\infty} H^{(2)}(f_0,\Delta f)X^*(f_0-\frac{\Delta f}{2})X(f_0+\frac{\Delta f}{2})df_0$	(24)
Cross-spectrum		Cross-bi-spectrum	
$S_{xy}(f) = 1/T\langle X^*(f)Y(f)\rangle$	(25)	$S_{xxy}(f_1,f_2) = \frac{1}{T}\langle\chi(f_1,f_2)\rangle = \frac{1}{T}\langle X(f_1)X^*(f_2)Y(\Delta f)\rangle$	(26)
LTF estimation		QTF estimation	
$H^{(1)}(f) = \frac{S_{xy}(f)}{S_{xx}(f)}$	(27)	$H^{(2)}(f_1,f_2) = \frac{S_{xxy}(f_1,f_2)}{S_{xx}(f_1)S_{xx}(f_2)}$	(28)
Power spectrum output		Power spectrum output	
$S_{yy}(f) = \lvert H^{(1)}(f)\rvert^2 S_{xx}(f)$	(29)	$S_{yy}(\Delta f) = \int_{-\infty}^{\infty}\lvert H^{(2)}(f_0,\Delta f)\rvert^2 S_{xx}(f_0-\frac{\Delta f}{2})S_{xx}(f_0+\frac{\Delta f}{2})df_0$	(30)
Coherence function			
$C_{xy}(f) = \frac{S_{xy}(f)}{\sqrt{S_{xx}(f)S_{yy}(f)}}$	(31)		

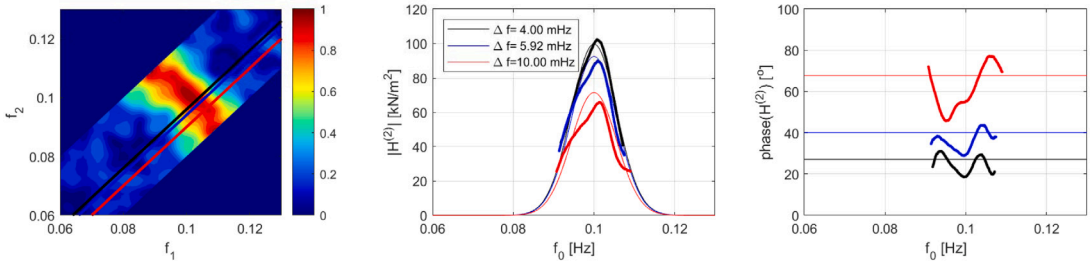

Fig. 7. Comparison of the amplitude (middle) and phase (right) of the estimated QTF $H^{(2)}$ (thick dots) and true QTF $\mathcal{H}^{(2)}$ (thin line). Left: $\xi(f_1,f_2)/\xi_{\max}$, and difference frequencies of interest, represented as diagonals of the bi-frequency plane.

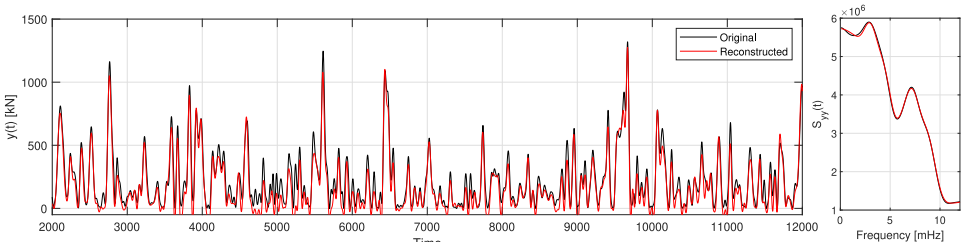

Fig. 8. Comparison between the original (black) and reconstructed (red) time series (left) and power spectra (right) for the original.

the analytical verification case. The agreement between the numerical and empirical QTFs is fair. A first amplitude peak is visible near the (uncoupled) eigenfrequency $f_{\text{heave}} = 0.088$ Hz. A second amplitude top can be observed at a mean frequency f_0, slightly beyond $f_{\text{pitch}} = 0.103$ Hz. Quantitatively, $|H^{(2)}|$ predicted by the numerical and empirical methods differ by less than 10% for $f_0 < f_{\text{pitch}}$, deteriorating when f_0 differs from the peak frequency of the wave spectrum. The phase angle of $H^{(2)}$ is rather small on the f_0 range of interest. For $f_0 > 0.1$ Hz and $\Delta f = 10$mHz, the numerical method predicts an increasing phase with f_0, which is captured by the cross-bi-spectral analysis, but at a slightly higher difference frequency (phase of +50 ° for $(f_0, \Delta f) = (0.14$ Hz,13 mHz)).

The numerical and experimental QTFs are used, together with the LF damping and added mass estimated empirically in Section 3.1, to reconstruct motions, for all external damping and restoring parameters listed in Table 2. These motions are compared in Fig. 10, with motions measured in the laboratory. Excellent agreement is found in this sea-state between measurements, numerical and empirical estimations. It is clear that the empirical (and numerical) QTF, combined with the LF added mass and damping estimated empirically lead to satisfactory estimates of the motions for whole range of mooring damping and stiffness, confirming the adequacy of the simplified hydrodynamic model (11) and estimated parameters. Note that the results (QTF and damping ratios) obtained in a systematic manner here are consistent with those obtained previously by the arguably less robust trial-and-error method described in Section 1 (deconvolution using guessed oscillator parameters) and used in Fonseca and Stansberg (2017).

5. Conclusion

We outlined a new method to estimate empirically the low-frequency damping, added-mass, and wave excitation load τ_w, which is of practical interest for the calibration of numerical models of floating structures. The proposed method alleviates issues related to the poor identifiability for systems with very narrow-banded response (due to e.g. little damping), enabling, in particular, to distinguish LF

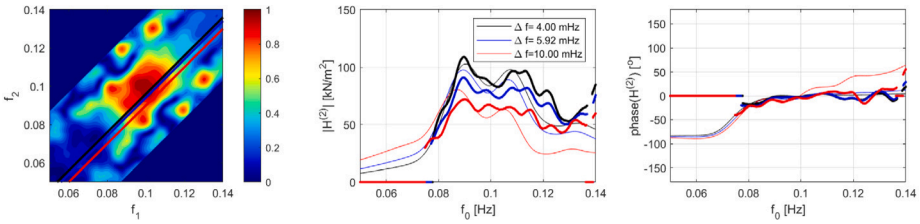

Fig. 9. Amplitude (middle) and phase (right) of the empirical QTF (thick dots) and numerical QTF (thin line). Left: $\xi(f_1, f_2)/\xi_{\max}$ and difference frequencies of interest.

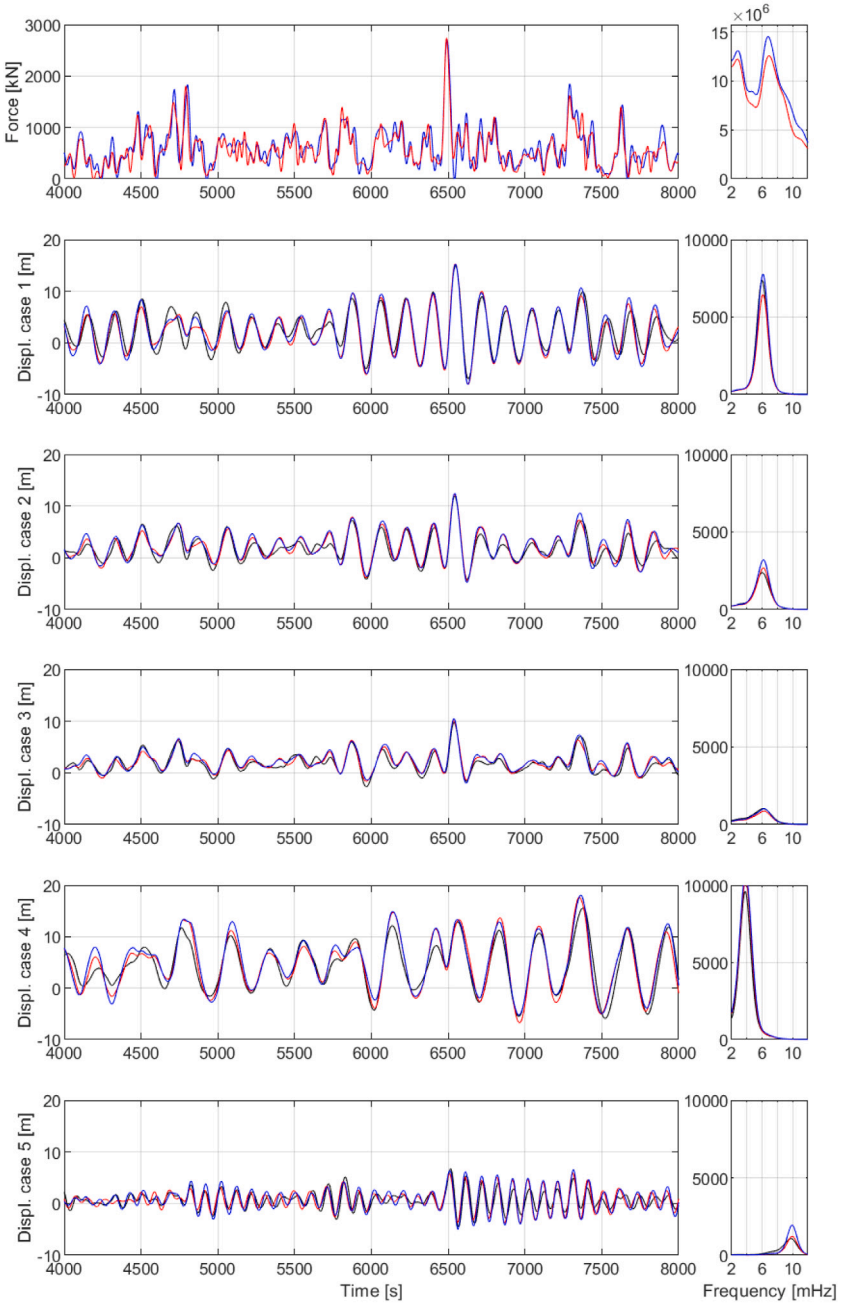

Fig. 10. Time series (left) and power spectrum (right) of the wave force (top) and resulting motions. Results obtained with the estimated empirical QTF are plotted in red, and with the numerical QTF in blue. In all cases, the LF damping and added-mass estimated empirically was used. Motions measurements are in black. The external stiffness and damping applied to each case 1–5 are listed in Table 2.

damping (response-dependent) from external excitation loads τ_w (assumed to be response-independent) in a robust manner. The frequency range on which τ_w is estimated reliably is increased as compared to traditional methods based on *passive* soft mooring, as the sensitivity of the setup can now be tuned. From τ_w, empirical difference-frequency

QTFs are established using cross-bi-spectral analysis, discarding automatically regions of the bi-frequency plane where comparatively little information is available from the experiments.

We validated the novel method by considering a previously-studied FPSO, undergoing surge motions in head seas. The estimated LF damping was found to be in agreement with previous experimental studies, and the estimated QTF was consistent with 2nd order potential theory, as expected for moderate sea-states and in absence of current. Good agreement between re-constructed and measured motions were obtained for a wide range of external damping and stiffness, which indicated that the simple model structure in Eq. (11), i.e. a linear oscillator excited by a second-order process, was adequate to model LF motions for the case at hand.

The advances presented here, were enabled by a newly developed active positioning system, that applies a freely-chosen and deterministic linear restoring and damping load based on LF motions only. This method can therefore be categorized as *cyber–physical*, or *hybrid*, in the same way as earlier developments made by the author and collaborators to study floating wind turbines (Sauder et al., 2016).

In Fonseca and Stansberg (2017), significant discrepancies between numerical and empirical QTFs were shown to appear in harsher sea-states (larger H_s) and in presence of current. Further work includes applying the present method to such conditions and to other types floaters for which viscous effects matter. Systematic studies employing this method will contribute to improve our understanding of the nature of nonlinear hydrodynamic loads and, in long term, enhance our modeling capabilities.

CRediT authorship contribution statement

Thomas Sauder: Conceptualization, Data curation, Formal analysis, Funding acquisition, Investigation, Methodology, Project administration, Software, Validation, Visualization, Writing – original draft, Writing – review & editing.

Declaration of competing interest

The authors declare that they have no known competing financial interests or personal relationships that could have appeared to influence the work reported in this paper.

Acknowledgments

This research has been funded by the Research Council of Norway through projects 194068/F40 and 254845/O80, and by Equinor through a bilateral project with SINTEF Ocean. The author would like to acknowledge the constructive input from colleagues in the course of this research, in particular Drs Stansberg, Fonseca, Rogne, Kaasen, Pákozdi, and Messrs. Laflèche and Tahchiev.

Appendix A. Isserlis' theorem

Let $A = \{\alpha_1, \dots, \alpha_N\}$ be a set of integers such that $1 \le \alpha_i \le d$ for all i, and let $X \in \mathbb{R}^d$ be a Gaussian vector with zero mean. If N is odd, then $\langle X_A \rangle = 0$. If N is even, then

$$\langle X_A \rangle = \sum_{\sigma \in \Pi(A)} \prod_{i \in A/\sigma} \langle X_{\alpha_i} X_{\alpha_{\sigma(i)}} \rangle \tag{A.1}$$

In particular, for $A = \{1, 2, 3, 4\}$ we have

$$\langle X_1 X_2 X_3 X_4 \rangle = \langle X_1 X_2 \rangle \langle X_3 X_4 \rangle + \langle X_1 X_3 \rangle \langle X_2 X_4 \rangle + \langle X_1 X_4 \rangle \langle X_2 X_3 \rangle \tag{A.2}$$

Appendix B. Fundamental equation of the cross-bi-spectral analysis

Proof that $S_{xxy}(f_1, f_2) = H^{(2)}(f_1, f_2) S_{xx}(f_1) S_{xx}(f_2)$. We denote $\chi(f_1, f_2) = X(f_1) X^*(f_2) Y(f_2 - f_1)$ the raw complex cross-bi-spectrum.

$$\begin{aligned}
\langle \chi(f_1, f_2) \rangle &= \langle X(f_1) X^*(f_2) Y(\Delta f) \rangle \\
&= \langle X(f_0 - \frac{\Delta f}{2}) X^*(f_0 + \frac{\Delta f}{2}) \left(\int_{-\infty}^{\infty} H^{(2)}(f_0', \Delta f) X^* \right. \\
&\quad \left. \times (f_0' - \frac{\Delta f}{2}) X(f_0' + \frac{\Delta f}{2}) d f_0' \right) \rangle \\
&= \langle \int_{-\infty}^{\infty} H^{(2)}(f_0', \Delta f) X(f_0 - \frac{\Delta f}{2}) X^* \\
&\quad \times (f_0 + \frac{\Delta f}{2}) X^*(f_0' - \frac{\Delta f}{2}) X(f_0' + \frac{\Delta f}{2}) d f_0' \rangle \\
&= \int_{-\infty}^{\infty} H^{(2)}(f_0', \Delta f) \langle X(f_0 - \frac{\Delta f}{2}) X^* \\
&\quad \times (f_0 + \frac{\Delta f}{2}) X^*(f_0' - \frac{\Delta f}{2}) X(f_0' + \frac{\Delta f}{2}) \rangle d f_0'
\end{aligned}$$

We now apply (A.2). Since $X(f_1)$ and $X(f_2)$ are uncorrelated if $|f_1 - f_2| \ge 1/T$, combinations of $f_0 + \frac{\Delta f}{2}$ and $f_0 - \frac{\Delta f}{2}$ factors vanish, and only the second term in (A.2) remains.

$$\begin{aligned}
\langle \chi(f_1, f_2) \rangle &= \int_{-\infty}^{\infty} H^{(2)}(f_0', \Delta f) \langle X(f_0 - \frac{\Delta f}{2}) X^*(f_0' - \frac{\Delta f}{2}) \rangle \\
&\quad \times \langle X^*(f_0 + \frac{\Delta f}{2}) X(f_0' + \frac{\Delta f}{2}) \rangle d f_0'
\end{aligned}$$

Again, correlation only if $|f_0' - f_0| < 1/T$, so the integrand is nonnull only on a Δf wide interval centered on f_0.

$$\begin{aligned}
\langle \chi(f_1, f_2) \rangle &= \frac{1}{T} H^{(2)}(f_1, f_2) \langle |X(f_1)|^2 \rangle \langle |X(f_2)|^2 \rangle \\
\langle \chi(f_1, f_2) \rangle &= \frac{1}{T} H^{(2)}(f_1, f_2) (T S_{xx}(f_1)) (T S_{xx}(f_2)) \\
S_{xxy}(f_1, f_2) &= \frac{1}{T} \langle \chi(f_1, f_2) \rangle = H^{(2)}(f_1, f_2) S_{xx}(f_1) S_{xx}(f_2)
\end{aligned}$$

Appendix C. Power spectrum of the output

Proof that $S_{yy}(\Delta f) := \frac{1}{T} \langle |Y(\Delta f)|^2 \rangle = \int_{-\infty}^{\infty} |H^{(2)}(f_0, \Delta f)|^2 S_{xx}(f_0 - \frac{\Delta f}{2}) S_{xx}(f_0 + \frac{\Delta f}{2}) d f_0$

$$\begin{aligned}
\langle |Y(\Delta f)|^2 \rangle &= \langle Y(\Delta f) Y^*(\Delta f) \rangle \\
&= \langle \int_{-\infty}^{\infty} H^{(2)}(f_0', \Delta f) X^*(f_0' - \frac{\Delta f}{2}) X(f_0' + \frac{\Delta f}{2}) d f_0' \int_{-\infty}^{\infty} H^{(2)*} \\
&\quad \times (f_0'', \Delta f) X(f_0'' - \frac{\Delta f}{2}) X^*(f_0'' + \frac{\Delta f}{2}) d f_0'' \rangle \\
&= \langle \iint_{-\infty}^{\infty} H^{(2)}(f_0', \Delta f) X^*(f_0' - \frac{\Delta f}{2}) X(f_0' + \frac{\Delta f}{2}) H^{(2)*}(f_0'', \Delta f) \\
&\quad \times X(f_0'' - \frac{\Delta f}{2}) X^*(f_0'' + \frac{\Delta f}{2}) d f_0' d f_0'' \rangle \\
&= \iint_{-\infty}^{\infty} H^{(2)}(f_0', \Delta f) H^{(2)*}(f_0'', \Delta f) \langle X^*(f_0' - \frac{\Delta f}{2}) X(f_0' + \frac{\Delta f}{2}) \\
&\quad \times X(f_0'' - \frac{\Delta f}{2}) X^*(f_0'' + \frac{\Delta f}{2}) \rangle d f_0' d f_0''
\end{aligned}$$

Applying (A.2) to the previous equation, the first term vanishes as $X^*(f_0' - \frac{\Delta f}{2})$ and $X(f_0' + \frac{\Delta f}{2})$ are always uncorrelated, and the third term $\langle X^*(f_0' - \frac{\Delta f}{2}) X^*(f_0'' + \frac{\Delta f}{2}) \rangle \langle X(f_0' + \frac{\Delta f}{2}) X(f_0'' - \frac{\Delta f}{2}) \rangle$ vanishes, due to the fact that $X(f')$ *and* $X(f'')$ are only correlated if $|f' - f''| < \Delta f$. Keeping only the second term, we obtain that

$$\begin{aligned}
\langle |Y(\Delta f)|^2 \rangle &= \iint_{-\infty}^{\infty} H^{(2)}(f_0', \Delta f) H^{(2)*}(f_0'', \Delta f) \langle X^*(f_0' - \frac{\Delta f}{2}) X \\
&\quad \times (f_0'' - \frac{\Delta f}{2}) \rangle \langle X(f_0' + \frac{\Delta f}{2}) X^*(f_0'' + \frac{\Delta f}{2}) \rangle d f_0' d f_0'' \\
&= 1/T \int_{-\infty}^{\infty} H^{(2)}(f_0, \Delta f) H^{(2)*}(f_0, \Delta f) \langle X^*(f_0 - \frac{\Delta f}{2}) X \\
&\quad \times (f_0 - \frac{\Delta f}{2}) \rangle \langle X(f_0 + \frac{\Delta f}{2}) X^*(f_0 + \frac{\Delta f}{2}) \rangle d f_0
\end{aligned}$$

$$= 1/T \int_{-\infty}^{\infty} |H^{(2)}(f_0, \Delta f)|^2 \langle |X(f_0 - \frac{\Delta f}{2})|^2 \rangle \times \langle |X(f_0 + \frac{\Delta f}{2})|^2 \rangle df_0$$

$$= T \int_{-\infty}^{\infty} |H^{(2)}(f_0, \Delta f)|^2 S_{xx}(f_0 - \frac{\Delta f}{2}) S_{xx}(f_0 + \frac{\Delta f}{2}) df_0$$

which proves the result.

Appendix D. Relationship between wave group envelope and unit QTF

Let $U(t)$ be the signal obtained when applying a unit one-sided difference-frequency QTF to an input $x(t)$

$$U(t) = \iint_{-\infty}^{\infty} H^{(2)}(f_1, f_2) X^*(f_1) X(f_2) e^{i2\pi(f_2 - f_1)t} df_1 df_2 \quad (D.1)$$

$$= 2 \iint_{0}^{\infty} X^*(f_1) X(f_2) e^{i2\pi(f_2 - f_1)t} df_1 df_2 \quad (D.2)$$

$$= 2 \iint_{0}^{\infty} X^*(f_1) e^{-i2\pi f_1 t} X(f_2) e^{i2\pi f_2 t} df_1 df_2 \quad (D.3)$$

$$= 2 \int_{0}^{\infty} X^*(f_1) e^{-i2\pi f_1 t} df_1 \int_{0}^{\infty} X(f_2) e^{i2\pi f_2 t} df_2 \quad (D.4)$$

$$= 2 \left(\int_{0}^{\infty} X(f) e^{i2\pi f t} df \right)^* \left(\int_{0}^{\infty} X(f)^* e^{i2\pi f t} df \right) \quad (D.5)$$

$$= 2 \left| \left(\int_{0}^{\infty} X(f) e^{i2\pi f t} df \right) \right|^2 = \frac{1}{2} \left| \left(\int_{0}^{\infty} 2X(f) e^{i2\pi f t} df \right) \right|^2 \quad (D.6)$$

$$= \frac{1}{2} \left| \left(\int_{-\infty}^{\infty} X_A(f) e^{i2\pi f t} df \right) \right|^2 = \frac{1}{2} |x_A(t)|^2 \quad (D.7)$$

where x_A is the (complex) analytic signal, whose real part is $x(t)$ and imaginary part is the Hilbert transform of $x(t)$. The module of x_A is classically denoted the envelope of x. The Fourier components of x_A are null for negative frequencies, and twice those of x for positive frequencies.

References

Aksnes, V., Berthelsen, P.A., Da Fonseca, N.M.M.D., 2015. On the need for calibration of numerical models of large floating units against experimental data. In: The Twenty-Fifth International Ocean and Polar Engineering Conference. International Society of Offshore and Polar Engineers.

Bendat, J.S., Piersol, A.G., 2010. Random Data: Analysis and Measurement Procedures, fourth ed. In: Wiley Series in Probability and Statistics, Wiley, Hoboken, N.J.

Bunnik, T., Huijsmans, R., Namba, Y., 2006. Identification of quadratic responses of floating structures in waves. In: The Sixteenth International Offshore and Polar Engineering Conference. International Society of Offshore and Polar Engineers.

de Hauteclocque, G., Rezende, F., Waals, O., Chen, X.-B., 2012. Review of approximations to evaluate second-order low-frequency load. In: Volume 1: Offshore Technology. American Society of Mechanical Engineers, Rio de Janeiro, Brazil, pp. 363–371. http://dx.doi.org/10.1115/OMAE2012-83407.

Engebretsen, E., Pan, Z., Fonseca, N., 2020. Second-order difference-frequency loads on FPSOs by full QTF and relevant approximations. In: Volume 1: Offshore Technology. American Society of Mechanical Engineers, Virtual, Online, http://dx.doi.org/10.1115/OMAE2020-18132.

Faltinsen, O.M., 1993. Sea Loads on Ships and Offshore Structures. In: Cambridge Ocean Technology Series.

Fonseca, N., Ommani, B., Stansberg, C., Bøckmann, A., Birknes-Berg, J., Nestegård, A., de Hauteclocque, G., Baarholm, R., 2017. Wave forces and low frequency drift motions in extreme seas: benchmark studies. In: Offshore Technology Conference. Offshore Technology Conference, Houston, Texas, USA, http://dx.doi.org/10.4043/27803-MS.

Fonseca, N., Stansberg, C.T., 2017. Wave drift forces and low frequency damping on the exwave FPSO. In: Proceedings of the ASME 2017 36th International Conference on Ocean, Offshore and Arctic Engineering. http://dx.doi.org/10.1115/OMAE2017-62540.

Fossen, T.I., 2011. Handbook of Marine Craft Hydrodynamics and Motion Control. John Wiley & Sons, Ltd.

Fossen, T.I., Strand, J.P., 1999. Passive nonlinear observer design for ships using Lyapunov methods: Full-scale experiments with a supply vessel. Automatica 35 (1), 3–16. http://dx.doi.org/10.1016/S0005-1098(98)00121-6.

Grue, J., Palm, E., 1996. Wave drift damping of floating bodies in slow yaw motion. J. Fluid Mech. 319 (-1), 323. http://dx.doi.org/10.1017/S0022112096007367.

Kim, N., 2004. Extraction of the Second-Order Nonlinear Response from Model Test Data in Random Seas and Comparison of the Gaussian and Non-Gaussian Models (Ph.D. thesis). Texas A&M University.

Kinoshita, T., Bao, W., Yoshida, M., Ishibashi, K., 2002. Wave-drift added mass of a cylinder array free to respond to the incident waves. In: 21st International Conference on Offshore Mechanics and Arctic Engineering, Volume 4. Oslo, Norway, pp. 645–652. http://dx.doi.org/10.1115/OMAE2002-28442.

Molin, B., 2002. Hydrodynamique Des Structures Offshore. Editions Technip, Paris.

Ommani, B., Fonseca, N., Stansberg, C.T., 2017. Simulation of low frequency motions in severe seastates accounting for wave-current interaction effects. In: ASME 2017 36th International Conference on Ocean, Offshore and Arctic Engineering. Trondheim, Norway, http://dx.doi.org/10.1115/OMAE2017-62550.

Pinkster, J., 1979. Mean and low frequency wave drifting forces on floating structures. Ocean Eng. 6 (6), 593–615. http://dx.doi.org/10.1016/0029-8018(79)90010-6.

Pinkster, J., 1980. Low Frequency Second Order Wave Excitation Forces on Floating Structures (Ph.D. thesis). Delft University of Technology.

Pinkster, J., Huijsmans, R., 1992. Wave drift forces in shallow water. In: BOSS.

Rogne, Ø.Y., Haug, N., Lø ken, R., 2016. An improved method for model test based identification of drift coefficients and damping for floating platforms. In: Offshore Technology Conference.

Rugh, W.J., 1981. Nonlinear System Theory: the Volterra/Wiener Approach. The Johns Hopkins University Press.

Sauder, T., Chabaud, V., Thys, M., Bachynski, E.E., Sæther, L.O., 2016. Real-time hybrid model testing of a braceless semi-submersible wind turbine. part i: the hybrid approach. In: ASME 2016 35th International Conference on Ocean, Offshore and Arctic Engineering.

Sauder, T., Tahchiev, G., 2020. From soft mooring system to active positioning in laboratory experiments. In: Proceedings of the ASME 2020 39th International Conference on Ocean, Offshore and Arctic Engineering.

Stansberg, C.T., 1997. Linear and nonlinear system identification in model testing. In: International Conference on Non-Linear Aspects of Physical Model Tests. OTRC, Texas A&M University, Collage Station, Texas, USA.

Ueland, E., Sauder, T., Skjetne, R., 2021. Force tracking using actuated winches with position-controlled motors for use in hydrodynamical model testing. IEEE Access 1. http://dx.doi.org/10.1109/ACCESS.2021.3083539.

Vilsen, S., Sauder, T., Sø rensen, A.J., 2017. Real-time hybrid model testing of moored floating structures using nonlinear finite element simulations. In: Dynamics of Coupled Structures. In: Conference Proceedings of the Society for Experimental Mechanics Series, vol. 4, Springer International Publishing, pp. 79–92.

Yoshida, M., Kinoshita, T., Bao, W., 2005. Nonlinear hydrodynamic forces on an accelerated body in waves. J. Offshore Mech. Arct. Eng. 127.